Impacts of aerosol-photolysis interaction and aerosol-radiation feedback on surface-layer ozone in North China during multi-pollutant air pollution episodes

Hao Yang[1], Lei Chen[1], Hong Liao[1], Jia Zhu[1], Wenjie Wang[2], Xin Li[2]

[1]Jiangsu Key Laboratory of Atmospheric Environment Monitoring and Pollution Control, Jiangsu Collaborative Innovation Center of Atmospheric Environment and Equipment Technology, School of Environmental Science and Engineering, Nanjing University of Information Science & Technology, Nanjing 210044, China

[2]State Joint Key Laboratory of Environmental Simulation and Pollution Control, College of Environmental Sciences and Engineering, Peking University, Beijing 100871, China

Correspondence: Lei Chen (chenlei@nuist.edu.cn) and Hong Liao (hongliao@nuist.edu.cn)

Abstract

We examined the impacts of aerosol-radiation interactions, including the effects of aerosol-photolysis interaction (API) and aerosol-radiation feedback (ARF), on surface-layer ozone (O_3) concentrations during four multi-pollutant air pollution episodes characterized by high O_3 and $PM_{2.5}$ levels during 28 July to 3 August 2014 (Episode1), 8-13 July 2015 (Episode2), 5-11 June 2016 (Episode3), and 28 June to 3 July 2017 (Episode4) in North China, by using the Weather Research and Forecasting with Chemistry (WRF-Chem) model embedded with an integrated process analysis scheme. Our results show that API and ARF reduced the daytime shortwave radiative fluxes at the surface by 92.4~102.9 W m^{-2} and increased daytime shortwave radiative fluxes in the atmosphere by 72.8~85.2 W m^{-2}, as the values were averaged over the complex air pollution areas (CAPAs) in each of the four episodes. As a result, the stabilized atmosphere decreased the daytime planetary boundary layer height and 10 m wind speed by 129.0~249.0 m and 0.05~0.15 m s^{-1}, respectively, in CAPAs in the four episodes. Aerosols were simulated to reduce the daytime near-surface photolysis rates of J[NO_2] and J[O^1D] by 1.8×10^{-3}~2.0×10^{-3} s^{-1} and 5.7×10^{-6}~6.4×10^{-6} s^{-1}, respectively, in CAPAs in the four episodes. All the four episodes show the same conclusion that the reduction in O_3 by API is larger than that by ARF. API (ARF) was simulated to change daytime surface-layer O_3 concentrations by -8.5 ppb (-2.9 ppb), -10.3 ppb (-1.0 ppb), -9.1 ppb (-0.9 ppb) and -11.4 ppb (+0.7 ppb) in CAPAs of the four episodes, respectively. Process analysis indicated that the weakened O_3 chemical production made the greatest contribution to API effect, while the reduced vertical mixing was the key process for ARF effect. Our conclusions suggest that future $PM_{2.5}$ reductions may lead to O_3 increases due to the weakened aerosol-radiation interactions, which should be considered in air quality planning.

1 Introduction

The characteristics of air pollution in China during recent years are changing from the single pollutant (e.g., $PM_{2.5}$, particulate matter with an aerodynamic equivalent diameter of 2.5 μm or less) to multiple pollutants (e.g., $PM_{2.5}$ and ozone (O_3)) (Zhao et al., 2018; Zhu et al., 2019), and the synchronous occurrence of high $PM_{2.5}$ and O_3 concentrations has been frequently observed, especially during the warm seasons (Dai et al., 2021; Qin et al., 2021). Qin et al. (2021) reported that the co-occurrence of $PM_{2.5}$ and O_3 pollution days (days with $PM_{2.5}$ concentration > 75 μg m^{-3} as well as maximum daily 8 h average ozone concentration > 80 ppb) exceeded 324 days in eastern China during 2015-2019. Understanding the complex air pollution is essential for making plans to improve air quality in China.

Aerosols can influence O_3 by changing meteorology through absorbing and scattering solar radiation (defined as aerosol-radiation feedback (ARF) in this work) (Albrecht et al., 1989; Haywood et al., 2000; Lohmann et al., 2005), which influences air quality by altering the chemical reactions, transport and deposition of the pollutant (Gao et al., 2018; Qu et al., 2021; Xing et al., 2017; Zhang et al., 2018). Many studies examined the feedback between aerosols and meteorology (Gao et al., 2015; Gao et al., 2016a; Qiu et al., 2017; Chen et al., 2019; Zhu et al., 2021). For example, Gao et al. (2015) used the WRF-Chem model to investigate the feedbacks between aerosols and meteorological variables over the North China Plain in January 2013, and pointed out that aerosols caused a decrease in surface temperature by 0.8-2.8 °C but an increase of 0.1-0.5 °C around 925 hPa. By using the same WRF-Chem model, Qiu et al. (2017) reported that the surface downward shortwave radiation and PBLH were reduced by 54.6 W m^{-2} and 111.4 m, respectively, due to aerosol direct radiative effect during 21-27 February 2014 in the North China Plain. Such aerosol-induced changes in meteorological fields are expected to influence O_3 concentrations during multi-pollutant episodes with high concentrations of air pollutants.

Aerosols can also influence O_3 by altering photolysis rates (defined as aerosol-photolysis interaction (API) in this work) (Dickerson et al., 1997; Liao et al., 1999; Li

73 et al., 2011; Lou et al., 2014). Dickerson et al. (1997) reported that the presence of

74 pure scattering aerosol increased ground level ozone in the eastern United States by

75 20 to 45 ppb, while the presence of strongly absorbing aerosol reduced ground level

76 ozone by up to 24 ppb. Wang et al. (2019) found that aerosols reduced the net ozone

77 production rate by 25% by reducing the photolysis frequencies during a

78 comprehensive ~~filed~~field observation in Beijing in August 2012. Such aerosol-

79 induced changes in photolysis rates are expected to influence O_3 concentrations

80 during multi-pollutant episodes with high concentrations of air pollutants.

81   Few previous studies quantified the effects of ARF and API on O_3 concentrations.

82 Xing et al. (2017) applied a two-way online coupled WRF-CMAQ model and

83 reported that the combination of API and ARF reduced the surface daily maximum 1

84 h O_3 (MDA1 O_3) by up to 39 µg m^{-3} over China during January 2013. Qu et al. (2021)

85 found, by using the UK Earth System Model (UKESM1), that ARF reduced the

86 annual average surface O_3 by 3.84 ppb (14.9%) in the North China Plain during 2014.

87 Gao et al. (2020) analyzed the impacts of API on O_3 by using the WRF-Chem model

88 and reported that API reduced surface O_3 by 10.6 ppb (19.0%), 8.6 ppb (19.4%), and

89 8.2 ppb (17.7%) in Beijing, Tianjin, and Shijiazhuang, respectively, during October

90 2018. However, these previous studies mostly examined either ARF or API and did

91 not examine their total and respective roles in O_3 pollution in China. Furthermore,

92 these previous studies lacked process understanding about the impacts of ARF and

93 API on O_3 pollution under co-occurrence of $PM_{2.5}$ and O_3 pollution events.

94   The present study aims to quantify the respective/combined impacts of ARF and

95 API on surface O_3 concentrations by using the WRF-Chem model, and to identify the

96 prominent physical and/or chemical processes responsible for ARF and API effects by

97 using an integrated process rate (IPR) analysis embedded in the WRF-Chem model.

98 We carry on simulations and analyses on four multi-pollutant air pollution episodes

99 (Episode1: 28 July to 3 August 2014; Episode2: 8-13 July 2015; Episode3: 5-11 June

100 2016; Episode4, 28 June to 3 July 2017) in North China with high O_3 and $PM_{2.5}$ levels

101 (the daily mean $PM_{2.5}$ and the maximum daily 8-h average O_3 concentration are larger

102 than 75 µg m^{-3} and 80 ppb, respectively). These episodes are selected because (1)

103 these events with high concentrations of both $PM_{2.5}$ and O_3 are the major subjects of

104 air pollution control, (2) high concentrations of both $PM_{2.5}$ and O_3 allow one to obtain

105 the strongest signals of ARF and API, (3) the measurements of $J[NO_2]$ during 2014

106 and 2015 from Peking University site (Wang et al., 2019) can help to constrain the

107 simulated photolysis rates of NO_2, and (4) selected events cover different years of

108 2014 to 2017 during which the governmental Air Pollution Prevention and Control

109 Action Plan was implemented (the changes in emissions and observed $PM_{2.5}$ in the

110 studied region during 2014-2017 are shown in Fig. S1). We expect that the

111 conclusions obtained from multiple episodes represent the general understanding of

112 the impacts of ARF and API.

113   The model configuration, numerical experiments, observational data, and the

114 integrated process rate analysis are described in section 2. Section 3 shows the model

115 evaluation. Results and discussions are presentedexhibited in section 4, and the

116 conclusions and discussions are summarizedprovided in section 5.

2 Methods

2.1 Model configuration

119   The version 3.7.1 of the online-coupled Weather Research and Forecasting with

120 Chemistry (WRF-Chem) model (Grell et al., 2005; Skamarock et al., 2008) is used in

121 this study to explore the impacts of aerosol-radiation interactions on surface-layer O_3

122 in North China. WRF-Chem can simulate gas phase species and aerosols coupled with

123 meteorological fields, and has been widely used to investigate air pollution over North

124 China (Gao et al., 2016a; Gao et al., 2020; Wu et al., 2020). As shown in Fig. 1, we

125 design two nested model domains with the number of grid points of 57 (west–east) ×

126 41 (south–north) and 37 (west–east) × 43 (south–north) at 27 and 9 km horizontal

127 resolutions, respectively. The parent domain centers at (39 °N, 117 °E). The model

128 contains 29 vertical levels from the surface to 50 hPa, with 14 levels below 2 km for

129 the fully description of the vertical structure of planetary boundary layer (PBL).

130   The Carbon Bond Mechanism Z (CBM-Z) is selected as the gas-phase chemical

131 mechanism (Zaveri and Peters, 1999), and the full 8-bin MOSAIC (Model for

Simulating Aerosol Interactions and Chemistry) aerosol module with aqueous chemistry is used to simulate aerosol evolution (Zaveri et al., 2008). The photolysis rates are calculated by the Fast-J scheme (Wild et al., 2000). Other major physical parameterizations used in this study are listed in Table 1.

The initial and boundary meteorological conditions are provided by the National Centers for Environmental Prediction (NCEP) Final Analysis data with a spatial resolution of $1° \times 1°$. In order to limit the model bias of simulated meteorological fields, the four-dimensional data assimilation (FDDA) is used with the nudging coefficient of 3.0×10^{-4} for wind, temperature and humidity (no analysis nudging is applied for the inner domain) (Lo et al., 2008; Otte, 2008). Chemical initial and boundary conditions are obtained from the Model for Ozone and Related chemical Tracers, version 4 (MOZART-4) forecasts (Emmons et al., 2010).

Anthropogenic emissions in these four episodes are taken from the Multi-resolution Emission Inventory for China (MEIC) (http://www.meicmodel.org/) (Li et al., 2017a). These emission inventories provide emissions of sulfur dioxide (SO_2), nitrogen oxides (NO_x), carbon monoxide (CO), non-methane volatile organic compounds (NMVOCs), carbon dioxide (CO_2), ammonia (NH_3), black carbon (BC), organic carbon (OC), PM_{10} (particulate matter with aerodynamic diameter is 10 µm and less) and $PM_{2.5}$. Emissions are aggregated from four sectors, including power generation, industry, residential, and transportation, with $0.25° \times 0.25°$ spatial resolution. Biogenic emissions are calculated online by the Model of Emissions of Gases and Aerosols from Nature (MEGAN) (Guenther et al., 2006).

2.2 Numerical experiments

To quantify the impacts of API and ARF on O_3, three experiments have been conducted: (1) BASE – the base simulation coupled with the interactions between aerosol and radiation, which includes both impacts of API and ARF; (2) NOAPI – the same as the BASE case, but the impact of API is turned off (aerosol optical properties are set to zero in the photolysis module), following Wu et al. (2020); (3) NOALL – both the impacts of API and ARF are turned off (removing the mass of aerosol species

when calculating aerosol optical properties in the optical module), following Qiu et al. (2017). The differences between BASE and NOAPI (i.e., BASE minus NOAPI) represent the impacts of API. The contributions from ARF can be obtained by comparing NOAPI and NOALL (i.e., NOAPI minus NOALL). The combined effects of API and ARF on O_3 concentrations can be quantitatively evaluated by the differences between BASE and NOALL (i.e., BASE minus NOALL).

All the experiments in Episode1, Episode2, Episode3 and Episode4 are conducted from 26 July to 3 August 2014, 6-13 July 2015, 3-11 June 2016, and 26 June to 3 July 2017, respectively, with the first 40 hours as the model spin-up in each case. Simulation results from the BASE cases of the four episodes are used to evaluate the model performance.

2.3 Observational data

Simulation results are compared with meteorological and chemical measurements. The surface-layer meteorological data (2 m temperature (T_2), 2 m relative humidity (RH_2), and 10 m wind speed (WS_{10})) with the temporal resolution of 3 h at ten stations (Table S1) are obtained from NOAA's National Climatic Data Center (https://gis.ncdc.noaa.gov/maps/ncei/cdo/hourly). The radiosonde data of temperature at 08:00 and 20:00 LST in Beijing (39.93 °N, 116.28 °E) are provided by the University of Wyoming (http://weather.uwyo.edu/). Observed hourly concentrations of $PM_{2.5}$ and O_3 at thirty-two sites (Table S2) in North China are collected from the China National Environmental Monitoring Center (CNEMC). The photolysis rate of nitrogen dioxide ($J[NO_2]$) measured at the Peking University site (39.99 °N, 116.31 °E) is also used to evaluate the model performance. More details about the measurement technique of $J[NO_2]$ can be found in Wang et al. (2019). The aerosol optical depth (AOD) at Beijing site (39.98°N, 116.38°E) is provided by AERONET (level 2.0, http://aeronet.gsfc.nasa.gov/). The AOD at 675 nm and 440 nm are used to derive the AOD at 550 nm to compare with the simulated ones.

2.4 Integrated process rate analysis

Integrated process rate (IPR) analysis has been widely used to quantify the

contributions of different processes to O_3 variations (Goncalves et al., 2009; Gao et al., 2016b; Tang et al., 2017; Gao et al., 2018). In this study, four physical/chemical processes are considered, including vertical mixing (VMIX), net chemical production (CHEM), horizontal advection (ADVH), and vertical advection (ADVZ). VMIX is initiated by turbulent process and closely related to PBL development, which influences O_3 vertical gradients. CHEM represents the net O_3 chemical production (chemical production minus chemical consumption). ADVH and ADVZ represent transport by winds (Gao et al., 2016b). In this study, we define ADV as the sum of ADVH and ADVZ.

3 Model evaluation

Reasonable representation of observed meteorological and chemical variables by the WRF-Chem model can provide foundation for evaluating the impacts of aerosols on surface-layer ozone concentrations. The model results presented in this section are taken from the BASE cases in the four episodes. The concentrations of air pollutants are averaged over the thirty-two observation sites in Beijing, Tianjin and Baoding. To ensure the data quality, the mean value for each time is calculated only when concentrations are available at more than sixteen sites, as ~~did~~ done in Li et al. (2019a).

3.1 Chemical simulations

Figure 2 shows the temporal variations of observed and simulated $PM_{2.5}$ and O_3 concentrations over North China for the four episodes. As shown in Fig. 2, the temporal variations of observed $PM_{2.5}$ can be well performed by the model with index of agreement (IOA) of 0.68, 0.68, 0.67 and 0.44 and normalized mean bias (NMB) of -19.2%, 4.1%, 30.4% and 13.9% during Episode1, Episode2, Episode3 and Episode4, respectively. The model also tracks well the diurnal variation of O_3 over the North China, with IOA of 0.89, 0.94, 0.92 and 0.87 and NMB of -12.0%, -0.4%, 1.6% and -13.8% for Episode1, Episode2, Episode3 and Episode4, respectively.

Figure S2 shows the correlation between observed and simulated AOD at 550 nm in Beijing. In the WRF-Chem model, the AOD at 550 nm are calculated by using the values at 400 and 600 nm according to the Angstrom exponent. Analyzing Fig. S2,

219 the model can reproduce the observed AOD with R of 0.7 and NMB of 7.9%.

3.2 Meteorological simulations

221   Figure 3 shows the time series of observed and simulated T_2, RH_2, WS_{10} and

222 $J[NO_2]$ during the four episodes. The observed T_2, RH_2, WS_{10} are averaged over the

223 ten meteorological observation stations, and the $J[NO_2]$ are measured at Peking

224 University. Most of the monitored $J[NO_2]$ in Episode3 and Episode4 are unavailable,

225 so the comparison of $J[NO_2]$ in Episode3 and Episode4 is not shown. Generally, the

226 model can depict the temporal variations of T_2 fairly well with IOA of 0.94~0.98 and

227 the mean bias (MB) of -1.9~-0.6 °C. For RH_2, the IOA and MB are 0.90~0.98 and -

228 6.5%~1.9%, respectively. Although WRF-Chem model overestimates WS_{10} with the

229 MB of 0.6~1.0 m s^{-1}, the IOA for WS_{10} is 0.70~0.83 and the root-mean-square error

230 (RMSE) is 0.9~1.5 m s^{-1}, which is smaller than the threshold of model performance

231 criteria (2 m s^{-1}) proposed by Emery et al. (2001). The positive bias in wind speed can

232 also be reproduced in other studies (Zhang et al., 2010; Gao et al., 2015; Liao et al.,

233 2015; Qiu et al., 2017). The predicted $J[NO_2]$ agrees well with the observations with

234 IOA of 0.98~0.99 and NMB of 6.8%~6.9%. We also conduct comparisons of

235 observed and simulated temperature profiles at 08:00 and 20:00 LST in Beijing during

236 the four episodes (Fig. S3). The vertical profiles of observed temperature can be well

237 captured by the model in these four complex air pollution episodes. Generally, the

238 WRF-Chem model can reasonably reproduce the temporal variations of observed

239 meteorological parameters.

4 Results

241   We examine the impacts of aerosol-radiation interactions on O_3 concentrations

242 with a special focus on the complex air pollution areas (CAPAs, Fig. S4) in the four

243 episodes, where the daily mean simulated $PM_{2.5}$ and MDA8 (maximum daily 8-h

244 average) O_3 concentrations are larger than 75 µg m^{-3} and 80 ppb, respectively, based

245 on the National Ambient Air Quality Standards (http://www.mee.gov.cn).

4.1 Impacts of aerosol-radiation interactions on meteorology

247   Figure 4 shows the impacts of aerosol-radiation interactions on shortwave

248   radiation at the surface (BOT_SW), shortwave radiation in the atmosphere

249   (ATM_SW), PBLH, and WS_{10} during the daytime (08:00-17:00 LST) from Episode1

250   to Episode4. Analyzing the results of the interactions between aerosol and radiation

251   (the combined impacts of API and ARF), BOT_SW is decreased over the entire

252   simulated domain in the four episodes with the decreases of 93.2 W m^{-2} (20.5%),

253   100.3 W m^{-2} (19.5%), 92.4 W m^{-2} (19.2%) and 102.9 W m^{-2} (20.7%) over CAPAs,

254   respectively. Contrary to the changes in BOT_SW, ATM_SW is increased

255   significantly in the four episodes with the increases of 72.8 W m^{-2} (25.3%), 85.2 W m^{-2}

256   ^{2} (29.0%), 73.7 W m^{-2} (26.4%) and 76.9 W m^{-2} (25.8%) over CAPAs, respectively.

257   The decreased BOT_SW perturbs the near-surface energy flux, which weakens

258   convection and suppresses the development of PBL (Li et al., 2017b). The mean

259   PBLHs over CAPAs are decreased by 129.0 m (13.0%), 249.0 m (20.9%), 224.6 m

260   (19.0%) and 227.0 m (20.9%), respectively. WS_{10} exhibits overall reductions over

261   CAPAs and is calculated to decrease by 0.12 m s^{-1} (3.6%), 0.05 m s^{-1} (1.6%),0.12 m s^{-1}

262   ^{1} (3.0%) and 0.15 m s^{-1} (4.3%), for the four episodes, respectively. We also examine

263   the changed meteorological variables caused by API and ARF respectively. As shown

264   in Fig. S5 and S6, API has little impact on meteorological variables; which means the

265   major contributor to the meteorology variability is ARF.

266   **4.2 Impacts of aerosol-radiation interactions on photolysis**

267   Figure 5 shows the spatial distributions of mean daytime surface-layer $PM_{2.5}$

268   concentrations simulated by BASE cases and the changes in $J[NO_2]$ and $J[O^1D]$ due

269   to aerosol-radiation interactions from Episode1 to Episode4. When the combined

270   impacts (API and ARF) are considered, $J[NO_2]$ and $J[O^1D]$ are decreased over the

271   entire domain in the four episodes, and the spatial patterns of changed $J[NO_2]$ and

272    $J[O^1D]$ are similar to that of simulated $PM_{2.5}$. Analyzing the four simulated episodes,

273   the surface $J[NO_2]$ averaged over CAPAs are decreased by 1.8×10^{-3} s^{-1} (40.5%), 2.0

274    $\times 10^{-3}$ s^{-1} (36.8%), 1.8×10^{-3} s^{-1} (36.0%), and 2.0×10^{-3} s^{-1} (38.0%), respectively. The

275   decreased surface $J[O^1D]$ over CAPAs are 6.1×10^{-6} s^{-1} (48.8%), 6.3×10^{-6} s^{-1}

276 (41.4%), 5.7×10^{-6} s^{-1} (44.6%), and 6.4×10^{-6} s^{-1} (46.9%), respectively. Figure S7

277 exhibits the impacts of API and ARF on surface J[NO$_2$] and J[O^{1}D]. Conclusions can

278 be summarized that J[NO$_2$] and J[O^{1}D] are significantly modified by API and little

279 affected by ARF.

4.3 Impacts of aerosol-radiation interactions on O$_3$

281 Figure 6 shows the changes in surface-layer O$_3$ due to API, ARF, and the

282 combined effects (denoted as ALL) from Episode1 to Episode4. As shown in Fig.

283 6(a1-a4), API alone leads to overall surface O$_3$ decreases over the entire domain with

284 average reductions of 8.5 ppb (10.2%), 10.3 ppb (11.8%), 9.1 ppb (11.2%), and 11.4

285 ppb (12.2%) over CAPAs in the four episodes, respectively. The changes can be

286 explained by the substantially diminished UV radiation due to aerosol loading, which

287 significantly weakens the efficiency of photochemical reactions and restrains O$_3$

288 formation. However, the decreased surface O$_3$ concentrations due to ARF are only 2.9

289 ppb (3.2%, Fig. 6(b1)), 1.0 ppb (1.1%, Fig. 6(b2)) and 0.9 ppb (1.0%, Fig. 6(b3)) for

290 the Episode1 to Episode3 but ARF increased surface O$_3$ concentrations by 0.7 ppb

291 (0.5%, Fig.6(b4)) during Episode4, which was caused by the enhancement of

292 chemical production (Fig. S10 and Section 4.4). All the episodes show same

293 conclusion that the reduction in O$_3$ by API is larger than that by ARF. Fig. 6(c1-c4)

294 presents the combined effects of API and ARF. Generally, aerosol-radiation

295 interactions decrease the surface O$_3$ concentrations by 11.4 ppb (13.7%), 11.3 ppb

296 (13.0%), 10.0 ppb (12.3%) and 10.7 ppb (11.6%) averaged over CAPAs in the four

297 episodes, respectively.

4.4 Influencing mechanism of aerosol-radiation interactions on O$_3$

299 Figure 7a shows mean results of the four episodes (Episode1, Episode2,

300 Episode3 and Episode4) in diurnal variations of simulated daytime surface-layer O$_3$

301 concentrations from BASE, NOAPI and NOALL cases averaged over CAPAs. All the

302 experiments (BASE, NOAPI and NOALL) present O$_3$ increases from 08:00 LST. It is

303 shown that the simulated O$_3$ concentrations in BASE case increase more slowly than

304 that in NOAPI and NOALL cases. To explain the underlying mechanisms of API and

305   ARF impacts on O_3, we quantify the variations in contributions of different processes

306   (ADV, CHEM, and VMIX) to O_3 by using the IPR analysis.

307   Figure 7b shows hourly surface O_3 changes induced by each physical/chemical

308   process (i.e., ADV, CHEM, and VMIX) in BASE case averaged from Episode1 to

309   Episode4. The significant positive contribution to the hourly variation in O_3 is

310   contributed by VMIX, and the contribution reaches the maximum at about 09:00 LST.

311   Since VMIX increases the surface O_3 concentrations by transporting O_3 from aloft

312   (where O_3 concentrations are high) to the surface layer (Tang et al., 2017; Xing et al.,

313   2017; Gao et al., 2018). The CHEM process makes negative contributions at around

314   09:00 and 16:00 LST, which means that the chemical consumption of O_3 is stronger

315   than the chemical production. At noon, the net chemical contribution turns to be

316   positive due to stronger solar UV radiation. The contribution from all the processes

317   (NET, the sum of VMIX, CHEM, and ADV) to O_3 variation is peaked at the noon and

318   then becomes weakened. After sunset (17:00 LST), the NET contribution turns to be

319   negative over CAPAs, leading to O_3 decrease.

320   Figure 7c shows the changes in hourly process contributions caused by API

321   averaged from Episode1 to Episode4. The chemical production of O_3 is suppressed

322   significantly due to aerosol impacts on photolysis rates. The weakened O_3 chemical

323   production decreases the contribution from CHEM, and results in a negative value of

324   CHEM_DIF (-3.44 ppb h^{-1}). In contrast to CHEM_DIF, the contribution from

325   changed VMIX (VMIX_DIF) to O_3 concentration due to API is always positive, and

326   the mean value is +3.26 ppb h^{-1}. The positive change in VMIX due to API may be

327   associated with the different vertical gradient of O_3 between BASE and NOAPI cases

328   (Gao et al., 2020), as shown in Fig. 8a. The impact of API on ADV process is

329   relatively small (-0.26 ppb h^{-1}). NET_DIF, namely the sum of VMIX_DIF,

330   CHEM_DIF and ADV_DIF, indicates the differences in hourly O_3 changes caused by

331   API. As shown in Fig. 7c, NET_DIF is almost negative during the daytime over

332   CAPAs with the mean value of -0.44 ppb h^{-1}. This is because the decreases in CHEM

333   and ADV are larger than the increases in VMIX caused by API; the O_3 decrease is

334   mainly attributed to the significantly decreased contribution from CHEM. The

maximum difference in O_3 between BASE and NOAPI appears at 11:00 LST with a value of -12.5 ppb (Fig. 7a).

Figure 7d shows the impacts of ARF on each physical/chemical process contribution to the hourly O_3 variation averaged from Episode1 to Episode4. At 08:00 LST, the change in VMIX due to ARF is large with a value of -3.5 ppb h^{-1}, resulting in a net negative variation with all processes considered. The decrease in O_3 reaches the maximum with the value of 5.0 ppb at around 08:00 LST over CAPAs (Fig. 7a). During 09:00 to 16:00 LST, the positive VMIX_DIF (mean value of +0.10 ppb h^{-1}) or the positive CHEM_DIF (mean value of +0.75 ppb h^{-1}) is the major process to positive NET_DIF. The positive VMIX_DIF is related to the evolution in boundary layer during the daytime. The VOCs/NO_x ratio is calculated to classify sensitivity regimes and to indicate the possible O_3 responses to changes in VOCs and/or NO_x concentrations. O_3 production is VOC-limited if the ratio is less than 4, and is NO_x-limited if the ratio is larger than 15 (Edson et al., 2017; Li et al., 2017c). The ratio of VOCs/NO_x ranging around 4-15 indicates a transitional regime, where ozone is nearly equally sensitive to both species (Sillman, 1999). As shown in Fig. S8, (a-f), O_3 is mainly formed under the VOC-limited and the transition regimes in CAPAs. As shown in Figs. S8(g-i) and S8(j-l), both the surface concentrations of VOCs and NO_x are increased when the impacts of ARF are considered. Thus, the contribution of CHEM in NOAPI is larger than that in NOALL.

When both impacts of API and ARF are considered, the variation pattern of the difference in hourly process contribution shown in Fig. 7e is similar to that in Fig. 7c, which indicates that API is the dominant factor to surface-layer O_3 reduction.

Figure 8 presents the vertical profiles of simulated daytime O_3 concentrations in three cases (BASE, NOAPI, and NOALL), and the differences in contributions from each physical/chemical process to hourly O_3 variations caused by API, ARF and the combined effects averaged over CAPAs from Episode1 to Episode4. As shown in Fig. 8a, the O_3 concentration is lower in BASE than that in other two scenarios (NOAPI and NOALL), especially at the lower 12 levels (below 801.8 m), owing to the impacts of aerosols (API and/or ARF).

The changes in each process contribution caused by API are presented in Fig. 8b. The contribution from CHEM_DIF is -2.1 ppb h^{-1} for the first seven layers (from 25.6 to 318.5 m). Conversely, the contribution from VMIX_DIF shows a positive value under the 318.5 m (between the first layer to the seventh layer) with the mean value of +1.8 ppb h^{-1}. The positive variation in VMIX due to API may be associated with the different vertical gradient of O$_3$ between BASE and NOAPI again. The contributions of changed advections (ADVH_DIF and ADVZ_DIF) are relatively small, with mean values of +0.03 and -0.18 ppb h^{-1} below the first seven layers, which may result from small impact of API on wind filed (Fig. S6(a4-d4)). The net difference is a negative value (-0.45 ppb h^{-1}); API leads to O$_3$ reduction not only nearly surface but also aloft.

Figure 8c shows the differences in O$_3$ budget due to ARF. When the ARF is considered, the vertical turbulence is weakened and the development of PBL is inhibited, which makes VMIX_DIF negative at the lower seven layers (below the 318.5 m) with a mean value of -0.69 ppb h^{-1}, but the variation in CHEM caused by ARF is positive with a mean value of +0.86 ppb h^{-1}. The enhanced O$_3$ precursors due to ARF can promote the chemical production of O$_3$ (Tie et al., 2009; Gao et al., 2018). The changes of ADVZ and ADVH (ADVZ_DIF and ADVH_DIF) caused by ARF are associated with the variations in wind filed. When ARF is considered, the horizontal wind speed is decreased (Fig. S9(a)), which makes ADVH_DIF positive at the lower twelve layers with a mean value of +0.30 ppb h^{-1}. However, ADVZ_DIF is negative at these layers with a mean value of -0.26 ppb h^{-1} because aerosol radiative effects decrease the transport of O$_3$ from the upper to lower layers (Fig. S9(b)).

In Fig. 8d, the pattern and magnitude of the differences in process contributions between BASE and NOALL are similar to those caused by API, indicating the dominate contributor of API on O$_3$ changes. The impacts of API on O$_3$ both near the surface and aloft are greater than those of ARF.

Figure S10 and S11 detailed show the influencing mechanism of aerosol-radiation interactions on O$_3$ in each episode. Similar variation characteristics can be found among the four episodes as the mean situation discussed above, with the larger impacts of API on O$_3$ both near the surface and aloft than those of ARF, indicating the

role of API is much larger than that of ARF during all the simulated episodes.

4.5 Discussions

We presented above the results from our simulations of multi-pollutant air pollution episodes. In order to make the conclusion be more general, we carried out simulations for three additional air pollution conditions, i.e., (1) $PM_{2.5}$ pollution alone (High_PM, with daily mean $PM_{2.5}$ concentration larger than 75 µg m^{-3}), (2) O_3 pollution alone (High_O$_3$, with the maximum daily 8-h average O_3 concentration larger than 80 ppb), and (3) neither $PM_{2.5}$ nor O_3 exceeded air quality standard (Low_POL, with daily mean $PM_{2.5}$ and the maximum daily 8-h average O_3 concentrations smaller than 75 µg m^{-3} and 80 ppb, respectively). For each condition of air pollution, we examined two episodes.

Figures S12 and S13 show the temporal variations of observed and simulated $PM_{2.5}$ and O_3 concentrations during 7-12 October 2014 (High_PM_Episode1), 7-11 April 2014 (High_PM_Episode2), 15-21 June 2017 (High_O$_3$_Episode1), 12-17 July 2017 (High_O$_3$_Episode2), 13-18 June 2016 (Low_POL_Episode1), and 13-17 July 2016 (Low_POL_Episode2). The temporal variations of observed $PM_{2.5}$ can be well captured by the model with IOAs of 0.63, 0.82, 0.56, 0.42, 0.76 and 0.54, and NMBs of 7.4%, 20.3%, -21.7%, -25.9%, 14.7% and -29.3% during High_PM_Episode1, High_PM_Episode2, High_O$_3$_Episode1, High_O$_3$_Episode2, Low_POL_Episode1, and Low_POL_Episode2, respectively. The model also simulates well the diurnal variation of O_3 over the North China, with IOAs of 0.87, 0.80, 0.87, 0.90, 0.84 and 0.86, and NMBs of -9.4%, -29.5%, -15.2%, -9.4%, 11.6% and 18.0% in these six episodes, respectively.

Figure 9 shows changes in daytime surface-layer O_3 due to API, ARF, and the combined effects (denoted as ALL) of High_PM_Episode1, High_PM_Episode2, High_O$_3$_Episode1, High_O$_3$_Episode2, Low_POL_Episode1, and Low_POL_Episode2. As summarized in Table 2, all the simulations confirm the same conclusion that the reduction in O_3 by API is larger than that by ARF. Averaged over the entire domain, the percentage reductions in O_3 by API and ARF are, respectively,

29.3% and 6.2% in High_PM_Episode1, 16.9% and 4.7% in High_PM_Episode2, 5.3% and 0.1% in High_O$_3$_Episode1, 4.5% and 0.1% in High_O$_3$_Episode2, 6.8% and 1.0% in Low_POL_Episode1, and 2.9% and 0.7% in Low_POL_Episode2. It's worth noting that the percentage reductions in O$_3$ from both API and ARF in High_PM episodes are 1.6~3.2 times the impacts in the complex episodes, while the impacts in cases of Low_POL and High_O$_3$ are 0.3~0.7 times the impacts of complex episodes."

5 Conclusions ~~and Discussions~~

In this study, the fully coupled regional chemistry transport model WRF-Chem is applied to investigate the impacts of aerosol-radiation interactions, including the impacts of aerosol-photolysis interaction (API) and the impacts of aerosol-radiation feedback (ARF), on O$_3$ during summertime complex air pollution episodes during 28 July to 3 August 2014 (Episode1), 8-13 July 2015 (Episode2), 5-11 June 2016 (Episode3) and 28 June to 3 July 2017 (Episode4). Three sensitivity experiments are designed to quantify the respective and combined impacts from API and ARF. Generally, the spatiotemporal distributions of observed pollutant concentrations and meteorological parameters can be captured fairly well by the model with index of agreement of 0.44~0.94 for pollutant concentrations and 0.70~0.99 for meteorological parameters.

Sensitivity experiments show that aerosol-radiation interactions decrease BOT_SW, WS$_{10}$, PBLH, J[NO$_2$], and J[O^{1}D] by 92.4~102.9 W m^{-2}, 0.05~0.15 m s^{-1}, 129.0~249.0 m, 1.8 × 10^{-3}~2.0 × 10^{-3} s^{-1}, and 5.7 × 10^{-6}~6.4 × 10^{-6} s^{-1} over CAPAs, and increase ATM_SW by 72.8~85.2 W m^{-2}, respectively. The changed meteorological variables and weakened photochemistry reaction further reduce surface-layer O$_3$ concentrations by ~~up to~~ 10.0~11.4 ppb, with relative changes of 74.6%~106.5% by API and of -6.5%~25.4% by ARF ~~contributing 74.6%~106.5% and -6.5%%~25.4%, respectively~~.

We further examine the influencing mechanism of aerosol-radiation interactions on O$_3$ by using integrated process rate analysis. API can directly affect O$_3$ by reducing the photochemistry reactions within the lower several hundred meters and therefore

amplify the O_3 vertical gradient, which promotes the vertical mixing of O_3. The reduced photochemistry reactions of O_3 weaken the chemical contribution and reduce surface O_3 concentrations, even though the enhanced vertical mixing can partly counteract the reduction. ARF affects O_3 concentrations indirectly through the changed meteorological variables, e.g., the decreased PBLH. The suppressed PBL can weaken the vertical mixing of O_3 by turbulence. Generally, the impacts of API on O_3 both near the surface and aloft are greater than those of ARF, indicating the dominant role of API on O_3 reduction related with aerosol-radiation interactions.

This study provides a detailed understanding of aerosol impacts on O_3 through aerosol-radiation interactions (including both API and ARF), with the general conclusion summarized as follows: when the impacts of aerosol-radiation interactions are considered, the changed meteorological variables and weakened photochemistry reaction can change surface-layer O_3 concentrations during the warm season, and the API is the dominant factor for O_3 reduction. The results can also imply that future $PM_{2.5}$ reductions may lead to O_3 increases due to weakened aerosol-radiation interactions. A recent study emphasized the need for controlling VOCs emissions to mitigate O_3 pollution (Li et al., 2019b). Therefore, tighter controls of O_3 precursors (especially VOCs emissions) are needed to counteract future O_3 increases caused by weakened aerosol-radiation interactions.

There are some limitations in this work. (1) In the current CBMZ and MOSAIC schemes, the formation of SOA (secondary organic aerosol) is not included (Gao et al., 2015; Chen et al., 2019). The absence of SOA can underestimate the impacts of API and ARF on O_3. Meanwhile, the lack of SOA may lead to weaker heterogeneous reactions to result in higher O_3 concentrations (Li et al., 2019c). The net effect of the two processes will be discussed and quantified in our future study. (2) The CNEMC network was built in 2013. Before 2013, the national observations of $PM_{2.5}$ and O_3 concentrations were not available, which make it difficult to select the time and area of complex air pollution events and to evaluate the model results. Based on observation data, we were mainly focused on impacts of ARF and API on surface O_3 during complex air pollution episodes from 2014 to 2017. Additional simulations of

High PM, High O_3, and Low POL support the conclusion obtained from the complex air pollution episodes that the reduction in O_3 by API is larger than that by ARF.

There are some limitations in this work:

(1) In the current CBMZ and MOSAIC schemes, the formation of SOA (secondary organic aerosol) is not included (Gao et al., 2015; Chen et al., 2019). The absence of SOA can underestimate the impacts of API and ARF on O_3. Meanwhile, the lack of SOA may lead to weaker heterogeneous reactions to result in higher O_3 concentrations (Li et al., 2019c). The net effect of the two processes will be discussed and quantified in our future study.

(2) We presented above the results from our simulations of multi-pollutant air pollution episodes. In order to show that the conclusion of this work can be applied to other conditions of air pollution, three additional situations are carried out, i.e., (1) $PM_{2.5}$ pollution alone (Episode_add1, the daily mean $PM_{2.5}$ concentration is larger than 75 μg m^{-3}), (2) neither $PM_{2.5}$ nor O_3 exceed air quality standard (Episode_add2, the daily mean $PM_{2.5}$ and maximum daily 8-h average O_3 concentration are smaller than 75 μg m^{-3} and 80 ppb, respectively), and (3) O_3 pollution alone (Episode_add3, the maximum daily 8-h average O_3 concentration is larger than 80 ppb). Detailed information about these three additional episodes is listed in the supporting information (Text S1 and Table S3). Analyzing Episode_add1, Episode_add2 and Episode_add3 in Fig. S13, API alone is simulated to reduce surface O_3 averaged over each episode and over the entire domain by 15.3 ppb (29.3%), 4.4 ppb (6.8%) and 4.5 ppb (5.3%), respectively, and ARF alone reduces surface O_3 by 3.9 ppb (6.2%), 0.6 ppb (1.0%), and 0.1 ppb (0.1%), respectively. All the results confirm the same conclusion that the reduction in O_3 by API is larger than that by ARF.

Data availability

The observed hourly surface concentrations of air pollutants are derived from the China National Environmental Monitoring Center (http://www.cnemc.cn). The observed surface meteorological data are obtained from NOAA's National Climatic Data Center (https://gis.ncdc.noaa.gov/maps/ncei/cdo/hourly). The radiosonde data are provided by the University of Wyoming (http://weather.uwyo.edu/). The photolysis rates of nitrogen dioxide in Beijing are provided by Xin Li (li_xin@pku.edu.cn). The aerosol optical depth in Beijing is obtained from the AERONET level 2.0 data collection (http://aeronet.gsfc.nasa.gov/). The simulation results can be accessed by contacting Lei Chen (chenlei@nuist.edu.cn) and Hong Liao (hongliao@nuist.edu.cn).

Author contributions

HY, LC, and HL conceived the study and designed the experiments. HY and LC performed the simulations and carried out the data analysis. JZ, WW, and XL provided useful comments on the paper. HY, LC, and HL prepared the paper with contributions from all co-authors.

Competing interests

The authors declare that they have no competing interests.

Acknowledgements

This work is supported by the National Key R&D Program of China (2019YFA0606804), the National Natural Science Foundation of China (42007195), the Meteorological Soft Science Program of China Meteorological Administration (2021ZZXM46), and the Postgraduate Research and Practice Innovation Program of Jiangsu Province (KYCX21_1014). We acknowledge the High Performance Computing Center of Nanjing University of Information Science & Technology for

539   their support of this work.

Reference

Albrecht, B. A.: Aerosols, cloud microphysics, and fractional cloudiness, Science, 245, 1227–1230, 1989.

Chen, F. and Dudhia, J.: Coupling an Advanced Land Surface – Hydrology Model with the Penn State – NCAR MM5 Modeling System. Part I: Model Implementation and Sensitivity, Mon. Weather Rev., 129(4), 569–585, 2001.

Chen, L., Zhu, J., Liao, H., Gao, Y., Qiu, Y., Zhang, M., Liu, Z., Li, N., and Wang, Y.: Assessing the formation and evolution mechanisms of severe haze pollution in the Beijing–Tianjin–Hebei region using process analysis, Atmos. Chem. Phys., 19, 10845–10864, https://doi.org/10.5194/acp-19-10845-2019, 2019.

Dai, H., Zhu, J., Liao, H., Li, J., Liang, M., Yang, Y., and Yue, X.: Co-occurrence of ozone and $PM_{2.5}$ pollution in the Yangtze River Delta over 2013–2019: Spatiotemporal distribution and meteorological conditions, Atmos. Res., 249, 105363, 2021.

Dickerson, R. R., Kondragunta, S., Stenchikov, G., Civerolo, K. L., Doddridge, B. G., and Holben, B. N.: The impact of aerosols on solar ultraviolet radiation and photochemical smog, Science, 278, 827-830, 10.1126/science.278.5339.827, 1997.

Edson, C. T., Ivan, H.-P. and Alberto, M.: Use of combined observational- and model-derived photochemical indicators to assess the O_3-NOx-VOC System sensitivity in urban areas, Atmosphere., 8, 22. https://doi.org/10.3390/atmos8020022, 2017.

Emery, C., Tai, E., and Yarwood, G.: Enhanced meteorological modeling and performance evaluation for two Texas ozone episodes, in: Prepared for the Texas Natural Resource Conservation Commission, ENVIRON International Corporation, Novato, CA, USA, 2001.

Emmons, L. K., Walters, S., Hess, P. G., Lamarque, J.-F., Pfister, G. G., Fillmore, D., Granier, C., Guenther, A., Kinnison, D., Laepple, T., Orlando, J., Tie, X., Tyndall, G., Wiedinmyer, C., Baughcum, S. L., and Kloster, S.: Description and evaluation of the Model for Ozone and Related chemical Tracers, version 4 (MOZART-4),

Geosci. Model Dev., 3, 43–67, doi:10.5194/gmd- 3-43-2010, 2010.

Foken, T.: 50 years of the Monin-Obukhov similarity theory, Bound.-Layer Meteor., 119, 431–437, 2006.

Gao, J., Li, Y., Zhu, B., Hu, B., Wang, L., and Bao, F.: What have we missed when studying the impact of aerosols on surface ozone via changing photolysis rates?, Atmos. Chem. Phys., 20, 10831–10844, https://doi.org/10.5194/acp-20-10831-2020, 2020.

Gao, J. H., Zhu, B., Xiao, H., Kang, H. Q., Pan, C., Wang, D. D., and Wang, H. L.: Effects of black carbon and boundary layer interaction on surface ozone in Nanjing, China, Atmos. Chem. Phys., 18, 7081–7094, https://doi.org/10.5194/acp-18-7081-2018, 2018.

Gao, M., Carmichael, G. R., Wang, Y., Saide, P. E., Yu, M., Xin, J., Liu, Z., and Wang, Z.: Modeling study of the 2010 regional haze event in the North China Plain, Atmos. Chem. Phys., 16, 1673–1691, doi:10.5194/acp-16-1673-2016, 2016a.

Gao, J., Zhu, B., Xiao, H., Kang, H., Hou, X., and Shao, P.: A case study of surface ozone source apportionment during a high concentration episode, under frequent shifting wind conditions over the Yangtze River Delta, China, Sci. Total Environ., 544, 853, https://doi.org/10.1016/j.scitotenv.2015.12.039, 2016b.

Gao, Y., Zhang, M., Liu, Z., Wang, L., Wang, P., Xia, X., Tao, M., and Zhu, L.: Modeling the feedback between aerosol and meteorological variables in the atmospheric boundary layer during a severe fog–haze event over the North China Plain, Atmos. Chem. Phys., 15, 4279–4295, doi:10.5194/acp-15-4279-2015, 2015.

Goncalves, M., Jimenez-Guerrero, P., Baldasano, J.M.: Contribution of atmospheric processes affecting the dynamics of air pollution in South-Western Europe during a typical summertime photochemical episode, Atmos. Chem. Phys., 9, 849 – 864, doi:10.5194/acp-9-849-2009, 2009.

Grell, G. A., Peckham, S. E., Schmitz, R., Mckeen, S. A., Frost, G., Skamarock, K., and Eder, B.: Fully coupled "online" chemistry within the WRF model, Atmos. Environ., 39, 6957–6975, 2005.

Guenther, A., Karl, T., Harley, P., Wiedinmyer, C., Palmer, P. I., and Geron, C.:

Estimates of global terrestrial isoprene emissions using MEGAN (Model of Emissions of Gases and Aerosols from Nature), Atmos. Chem. Phys., 6, 3181–3210, doi:10.5194/acp-6-3181-2006, 2006.

Haywood, J. and Boucher, O.: Estimates of the direct and indirect radiative forcing due to tropospheric aerosols: A review, Rev. Geophys., 38, 513–543, 2000.

Hong, S.-Y., Noh, Y., and Dudhia, J.: A New Vertical Diffusion Package with an Explicit Treatment of Entrainment Processes, Mon. Weather Rev., 134, 2318–2341, 2006.

Iacono, M. J., Delamere, J. S., Mlawer, E. J., Shephard, M. W., Clough, S. A., and Collins, W. D.: Radiative forcing by long-lived greenhouse gases: Calculations with the AER radiative transfer models, J. Geophys. Res., 113, D13103, doi:10.1029/2008JD009944, 2008.

Li, G., Bei, N., Tie, X., and Molina, L. T.: Aerosol effects on the photochemistry in Mexico City during MCMA-2006/MILAGRO campaign, Atmos Chem Phys, 11, 5169-5182, 10.5194/acp-11-5169-2011, 2011.

Li, J. D., Liao, H., Hu, J. L., Li, N.: Severe particulate pollution days in China during 2013-2018 and the associated typical weather patterns in Beijing-Tianjin-Hebei and the Yangtze River Delta regions, *Environmental Pollution*, 248, 74-81, 2019a.

Li, K., Jacob, D. J., Liao, H., Zhu, J., Shah, V., Shen, L., Bates, K. H., Zhang, Q., and Zhai, S.: A two-pollutant strategy for improving ozone and particulate air quality in China, Nat. Geosci., 12, 906–910, https://doi.org/10.1038/s41561-019-0464-x, 2019b.

Li, K., Jacob, D. J., Liao, H., Shen, L., Zhang, Q., and Bates, K. H.: Anthropogenic drivers of 2013–2017 trends in summer surface ozone in China, P. Natl. Acad. Sci. USA, 116, 422–427, https://doi.org/10.1073/pnas.1812168116, 2019c.

Li, M., Zhang, Q., Kurokawa, J.-I., Woo, J.-H., He, K., Lu, Z., Ohara, T., Song, Y., Streets, D. G., Carmichael, G. R., Cheng, Y., Hong, C., Huo, H., Jiang, X., Kang, S., Liu, F., Su, H., and Zheng, B.: MIX: a mosaic Asian anthropogenic emission inventory under the international collaboration framework of the MICS-Asia and HTAP, Atmos. Chem. Phys., 17, 935–963, https://doi.org/10.5194/acp-17-935-2017,

629   2017a.

630   Li, Z., Guo, J., Ding, A., Liao, H., Liu, J., Sun, Y., Wang, T., Xue, H., Zhang, H., and

631   Zhu, B.: Aerosol and boundary-layer interactions and impact on air quality, Nat. Sci.

632   Rev., 4, 810–833, https://doi.org/10.1093/nsr/nwx117, 2017b.

633   Li, K., Chen, L., Ying, F., White, S. J., Jang, C., Wu, X., Gao, X., Hong, S., Shen, J.,

634   Azzi, M. and Cen, K: Meteorological and chemical impacts on ozone formation: a

635   case study in Hangzhou, China, Atmos. Res., 196, https://doi.org/10.1016/

636   j.atmosres.2017.06.003, 2017c.

637   Liao, H., Yung, Y. L., and Seinfeld, J. H.: Effects of aerosols on tropospheric

638   photolysis rates in clear and cloudy atmospheres, J. Geophys. Res., 104, 23697–

639   23707, 1999.

640   Liao, L., Lou, S. J., Fu, Y., Chang, W. Y., and Liao, H.: Radiative forcing of aerosols

641   and its impact on surface air temperature on the synoptic scale in eastern China [in

642   Chinese], Chin. J. Atmos. Sci., 39, 68–82, doi: 10.3878/j.issn.1006-

643   9895.1402.13302, 2015.

644   Lin, Y.-L., Farley, R. D., and Orville, H. D.: Bulk parameterization of the snow field

645   in a cloud model, J. Clim. Appl. Meteorol., 22, 1065–1092, 1983.

646   Lo, J. C.-F., Yang, Z. L., and Pielke Sr, R. A.: Assessment of three dynamical climate

647   downscaling methods using the Weather Research and Forecasting (WRF) model, J.

648   Geophys. Res., 113, D09112, doi:10.1029/2007jd009216, 2008.

649   Lohmann, U., and Feichter, J.: Global indirect aerosol effects: A review. Atmospheric

650   Chemistry and Physics, 5, 715–737, https://doi.org/10.5194/acp-5-715-2005, 2005.

651   Lou, S., Liao, H., and Zhu, B.: Impacts of aerosols on surface-layer ozone

652   concentrations in China through heterogeneous reactions and changes in photolysis

653   rates, Atmos. Environ., 85, 123–138, 2014.

654   Otte, T. L.: The impact of nudging in the meteorological model for retrospective air

655   quality simulations. Part I: Evaluation against national observation networks. J.

656   Appl. Meteor. Climatol., 47, 1853–1867, 2008.

657   Qin, Y., Li, J., Gong, K., Wu, Z., Chen, M., Qin, M., Huang, L., and Hu, J.: Double

658   high pollution events in the Yangtze River Delta from 2015 to 2019: Characteristics,

659   trends, and meteorological situations, Sci. Total Environ., 792, 148349, 2021.

660   Qiu, Y., Liao, H., Zhang, R., and Hu, J.: Simulated impacts of direct radiative effects

661   of scattering and absorbing aerosols on surface layer aerosol concentrations in

662   China during a heavily polluted event in February 2014, J. Geophys. Res. Atmos.,

663   122, 5955–5975, doi:10.1002/2016JD026309, 2017.

664   Qu, Y., Voulgarakis, A., Wang, T., Kasoar, M., Wells, C., Yuan, C., Varma, S., and

665   Mansfield, L.: A study of the effect of aerosols on surface ozone through

666   meteorology feedbacks over China, Atmos. Chem. Phys., 21, 5705–5718,

667   https://doi.org/10.5194/acp-21-5705-2021, 2021.

668   Sillman, S.: The relation between ozone, NO_x and hydrocarbons in urban and polluted

669   rural environments, Atmos. Environ., 33, 1821-1845, https://doi.org/

670   10.1016/S1352-2310(98)00345-8, 1999.

671   Skamarock, W., Klemp, J. B., Dudhia, J., Gill, D. O., Barker, D. M., Duda, M., Huang,

672   X. Y., Wang,W., and Powers, J. G.: A description of the advanced research WRF

673   version 3, NCAR technical note NCAR/TN/u2013475, 2008.

674   Tang, G. Q., Zhu, X.W., Xin, J. Y., Hu, B., Song, T., Sun, Y., Zhang, J. Q., Wang, L. L.,

675   Cheng, M. T., Chao, N., Kong, L. B., Li, X., and Wang, Y. S.: Modelling study of

676   boundary-layer ozone over northern China – Part I: Ozone budget in summer,

677   Atmos. Res., 187, 128–137, 2017.

678   Tie, X., Geng, F., Li, P., Gao, W., and Zhao, C.: Measurement and modelling of ozone

679   variability in Shanghai, China, Atmos. Environ., 43, 4289–4302, 2009.

680   Wang, W., Li, X., Shao, M., Hu, M., Zeng, L., Wu, Y., and Tan, T.: The impact of

681   aerosols on photolysis frequencies and ozone production in Beijing during the 4-

682   year period 2012–2015, Atmos. Chem. Phys., 19, 9413–9429,

683   https://doi.org/10.5194/acp19-9413-2019, 2019.

684   Wild, O., Zhu, X., and Prather, M. J.: Fast-J: Accurate simulation of in- and below-

685   cloud photolysis in tropospheric chemical models, J. Atmos. Chem., 37, 245–282,

686   doi:10.1023/A:1006415919030, 2000.

687   Wu, J., Bei, N., Hu, B., Liu, S., Wang, Y., Shen, Z., Li, X., Liu, L., Wang, R., Liu, Z.,

688   Cao, J., Tie, X., Molina, L. T., Li, G.: Aerosol-photolysis interaction reduces

689   particulate matter during wintertime haze events, Proc. Natl. Acad. Sci. USA, 117,

690   9755–9761, 2020.

691 Xing, J., Wang, J. D., Mathur, R., Wang, S. X., Sarwar, G., Pleim, J., Hogrefe, C.,

692   Zhang, Y. Q., Jiang, J. K., Wong, D. and Hao, J. M.: Impacts of aerosol direct

693   effects on tropospheric ozone through changes in atmospheric dynamics and

694   photolysis rates, Atmos. Chem. Phys., 17, 9869–9883, https://doi.org/10.5194/acp-

695   17-9869-2017, 2017.

696 Zaveri, R. A. and Peters, L. K.: A new lumped structure photochemical mechanism

697   for large-scale applications, J. Geophys. Res., 104, D23, 30387–30415,

698   https://doi.org/10.1029/1999JD900876, 1999.

699 Zaveri, R. A., Easter, R. C., Fast, J. D., and Peters, L. K.: Model for simulating

700   aerosol interactions and chemistry (MOSAIC), J. Geophys. Res., 113, D13204,

701   https://doi.org/10.1029/2007JD008782, 2008.

702 Zhang, X., Zhang, Q., Hong, C. P., Zheng, Y. X., Geng, G. N., Tong, D., Zhang, Y. X.,

703   and Zhang, X. Y.: Enhancement of $PM_{2.5}$ concentrations by aerosol-meteorology

704   interactions over China. Journal of Geophysical Research: Atmospheres,123, 1179–

705   1194, https://doi.org/10.1002/2017JD027524, 2018.

706 Zhang, Y., Wen, X.-Y., and Jang, C. J.: Simulating chemistry–aerosol–cloud–

707   radiation–climate feedbacks over the continental US using the online-coupled

708   Weather Research Forecasting Model with chemistry (WRF/Chem), Atmos.

709   Environ., 44, 3568–3582, doi:10.1016/j.atmosenv.2010.05.056, 2010.

710 Zhao, H.; Zheng, Y., and Li, C. Spatiotemporal distribution of $PM_{2.5}$ and O_3 and their

711   interaction during the summer and winter seasons in Beijing, China. Sustainability,

712   10, 4519, 2018.

713 Zhu, J., Chen, L., Liao, H., and Dang, R.: Correlations between $PM_{2.5}$ and Ozone over

714   China and Associated Underlying Reasons, Atmosphere, 352, 1–15,

715   https://doi.org/10.3390/atmos10070352, 2019.

716 Zhu, J., Chen, L., Liao, H., Yang, H., Yang, Y., and Yue, X.: Enhanced $PM_{2.5}$

717   Decreases and O_3 Increases in China During COVID-19 Lockdown by Aerosol-

718   Radiation Feedback, Geophys. Res. Lett., 48,

https://doi.org/10.1029/2020GL090260, 2021.

1   **Table 1.** Physical parameterization options used in the simulation.

Options	Schemes
Microphysics scheme	Lin (Purdue) scheme (Lin et al.,1983)
Cumulus scheme	Grell 3D ensemble scheme
Boundary layer scheme	Yonsei University PBL scheme (Hong et al., 2006)
Surface layer scheme	Monin-Obukhov surface scheme (Foken, 2006)
Land-surface scheme	Unified Noah land-surface model (Chen and Dudhia, 2001)
Longwave radiation scheme	RRTMG (Iacono et al., 2008)
Shortwave radiation scheme	RRTMG (Iacono et al., 2008)

Table 2. Detailed information of the analyzed episodes, including the impacts of API, ARF and ALL on O_3 concentrations under different air pollution conditions. The numbers in bold indicate the concentrations exceeded the Class II limit of the National Ambient Air Quality Standards of China. The numbers in parentheses indicate the percentage changes in O_3 concentration.

Type	Episode	Time	PM$_{2.5}$ pollution (μg m^{-3})	O$_3$ pollution (ppb)	API (ppb)	ARF (ppb)	ALL (ppb)
Complex air pollution	Episode1	2014.7.28-2014.8.3	**113.3**	**80.0**	-8.5 (-10.2%)	-2.9 (-3.2%)	-11.4 (-13.7%)
	Episode2	2015.7.8-2015.7.13	**79.3**	**89.6**	-10.3 (-11.8%)	-1.0 (-1.1%)	-11.3 (-13.0%)
	Episode3	2016.6.5-2016.6.11	**76.5**	**87.6**	-9.1 (-11.2%)	-0.9 (-1.0%)	-10.0 (-12.3%)
	Episode4	2017.6.28-2017.7.3	**75.4**	**113.8**	-11.4 (-12.2%)	0.7 (0.5%)	-10.7 (-11.6%)
High_PM	Episode1	2014.10.7-2014.10.12	**223.5**	46.9	-15.3 (-29.3%)	-3.9 (-6.2%)	-19.2 (-37.6%)
	Episode2	2014.4.7-2014.4.11	**111.7**	54.8	-7.3 (-16.9%)	-2.4 (-4.7%)	-9.7 (-22.6%)
High_O$_3$	Episode1	2017.6.15-2017.6.21	61.9	**103.6**	-4.5 (-5.3%)	-0.1 (-0.1%)	-4.6 (-5.5%)
	Episode2	2017.7.12-2017.7.17	45.6	**100.4**	-3.8 (-4.5%)	-0.1 (-0.1%)	-3.9 (-4.6%)
Low_POL	Episode1	2016.6.13-2016.6.18	36.5	62.4	-4.4 (-6.8%)	-0.6 (-1.0%)	-5.0 (-7.9%)
	Episode2	2016.7.13-2016.7.17	38.3	55.9	-1.9 (-2.9%)	-0.5 (-0.7%)	-2.4 (-3.7%)
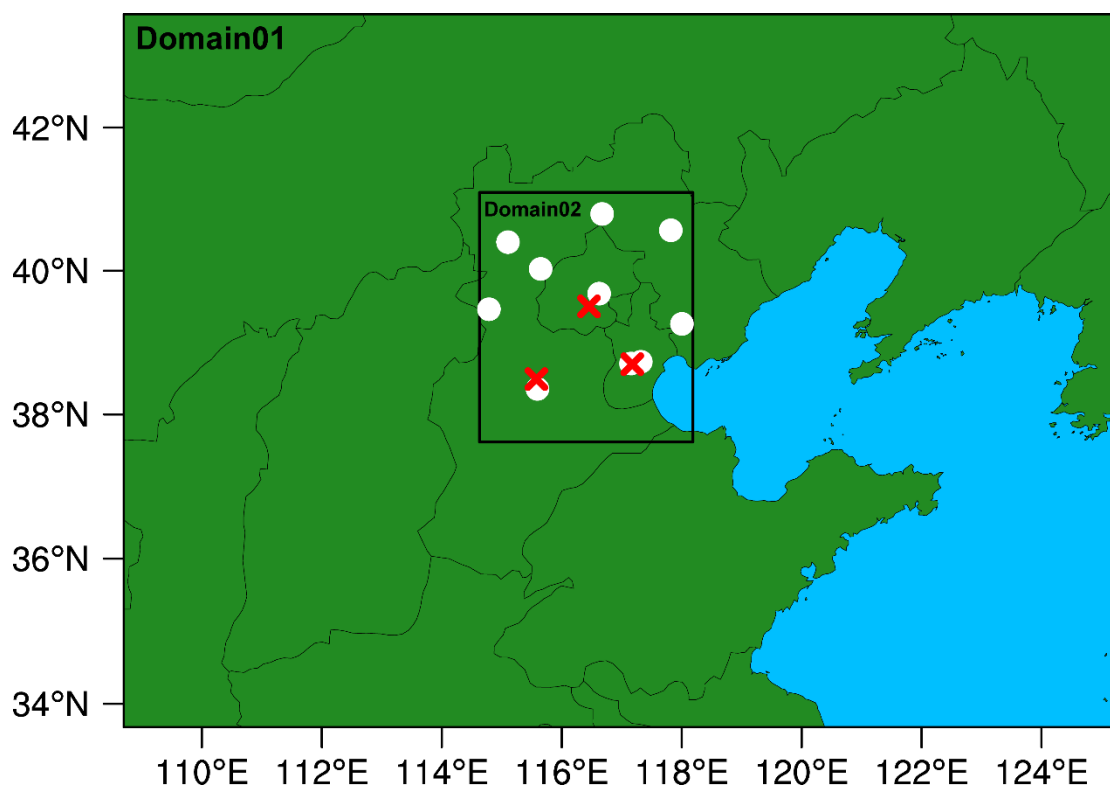
2 **Figure 1.** Map of the two WRF-Chem modeling domains with the locations of
3 meteorological (white dots) and environmental (red crosses) observation sites used for
4 model evaluation.
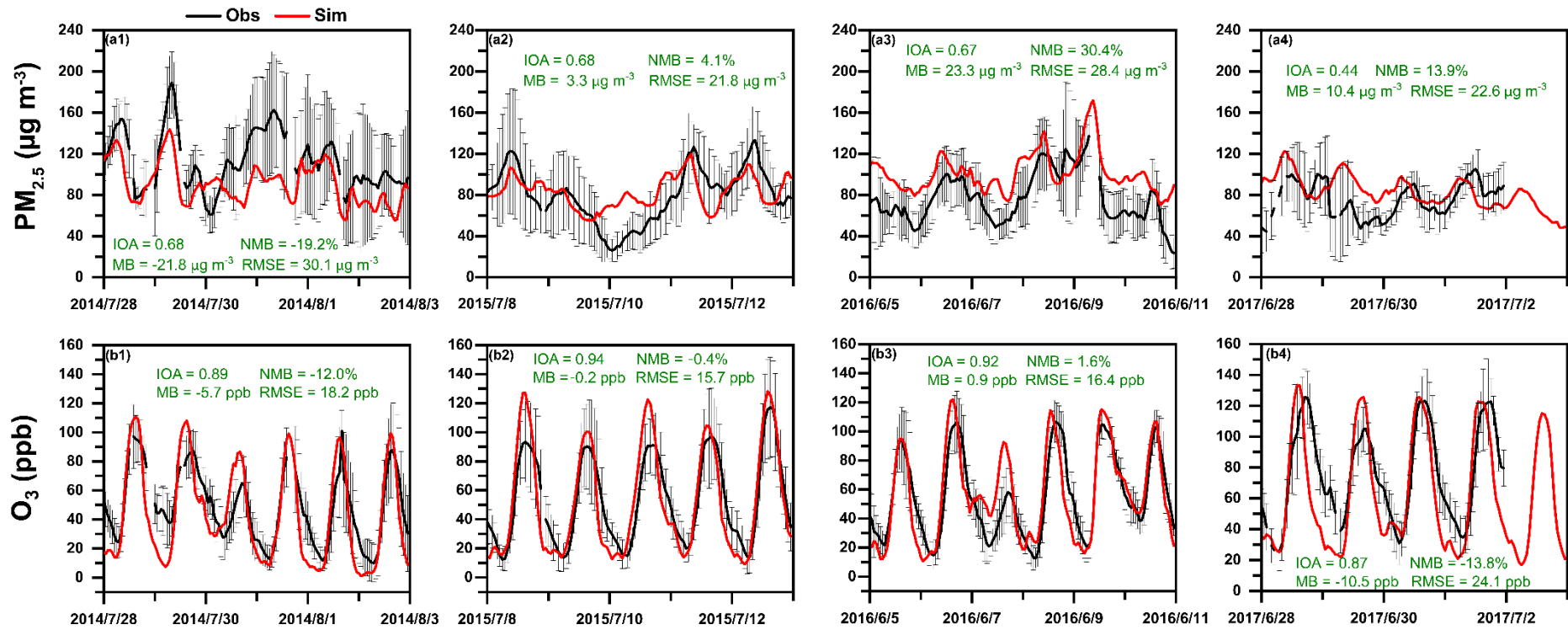
Figure 2. Time series of observed (black) and simulated (red) hourly surface (a) PM$_{2.5}$ and (b) O$_3$ concentrations averaged over the thirty-two observation sites in Beijing, Tianjin, and Baoding during 28 July to 3 August 2014 (Episode1, a1-b1), 8-13 July 2015 (Episode2, a2-b2), 5-11 June 2016 (Episode3, a3-b3) and 28 June to 3 July 2017 (Episode4, a4-b4). The error bars represent the standard deviations. The calculated index of agreement (IOA), mean bias (MB), normalized mean bias (NMB) and root-mean-square error (RMSE) are also shown.
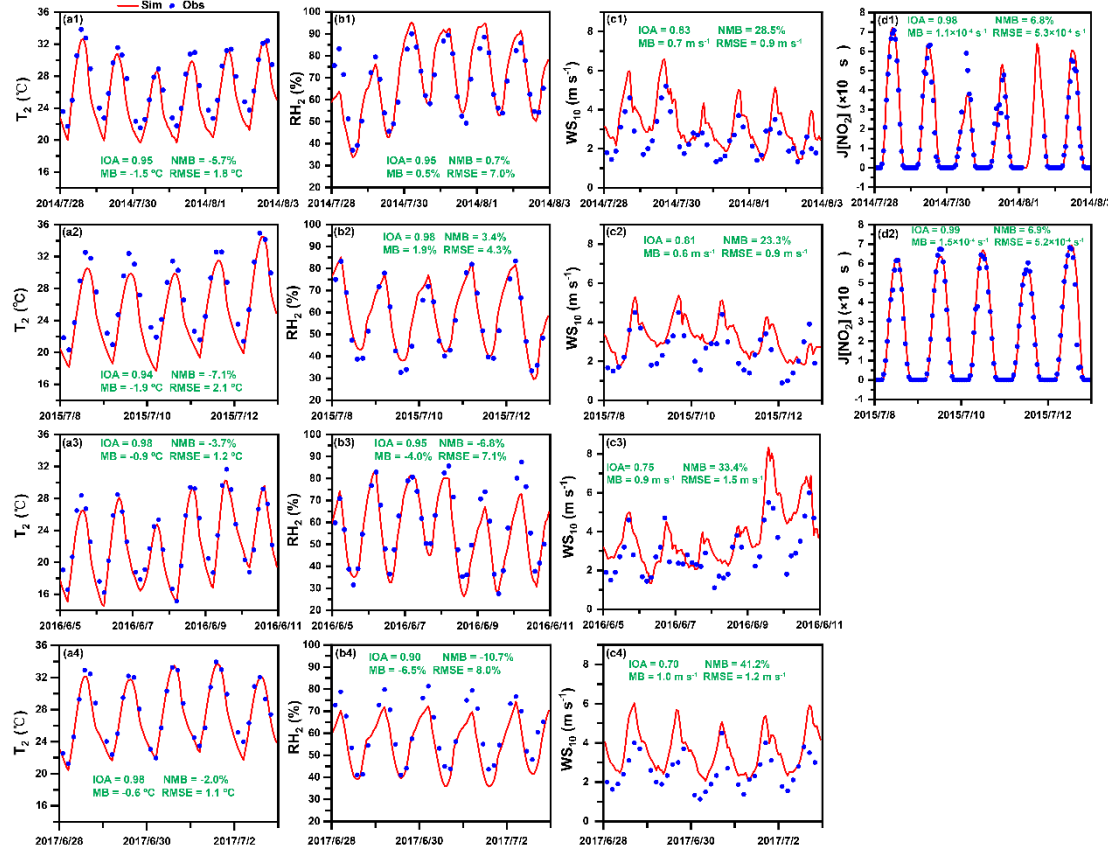
Figure 3. Time series of 3-hourly observed (blue dots) and hourly simulated (red lines) (a) 2-m temperature (T_2), (b) 2-m relative humidity (RH_2), (c) wind speed at 10 m (WS_{10}) averaged over ten meteorological observation stations, and (d) surface photolysis rate of NO_2 ($J[NO_2]$) during 28 July to 3 August 2014 (Episode1, a1-d1), 8-13 July 2015 (Episode2, a2-d2), 5-11 June 2016 (Episode3, a3-c3) and 28 June to 3 July 2017 (Episode4, a4-c4). The calculated index of agreement (IOA), mean bias (MB), normalized mean bias (NMB) and root-mean-square error (RMSE) are also shown.
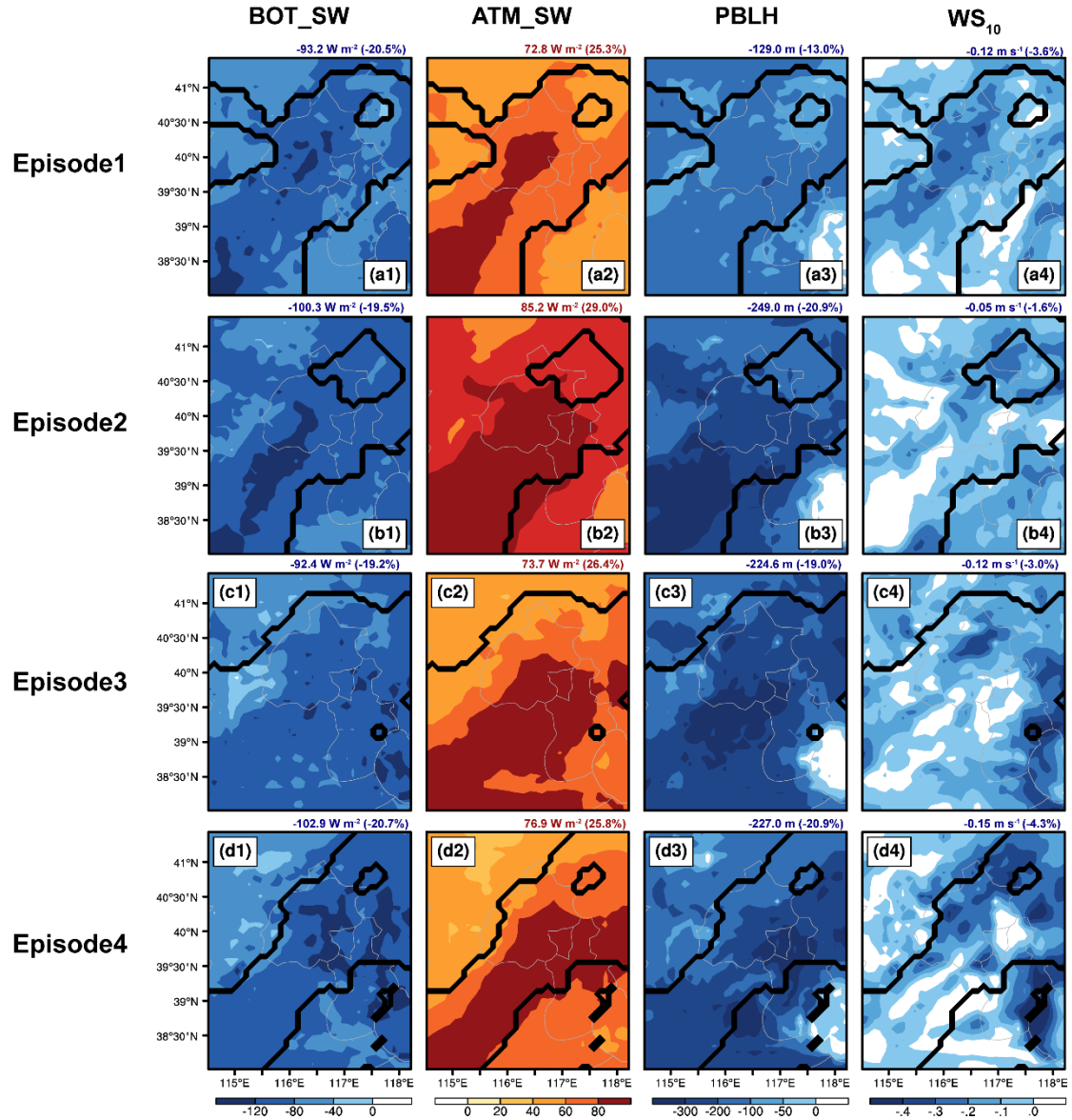
Figure 4. The impacts of aerosol-radiation interactions on shortwave radiation at the surface (BOT_SW), shortwave radiation in the atmosphere (ATM_SW), PBL height (PBLH), and 10-m wind speed (WS$_{10}$) in the daytime (08:00-17:00 LST) during 28 July to 3 August 2014 (Episode1), 8-13 July 2015 (Episode2), 5-11 June 2016 (Episode3) and 28 June to 3 July 2017 (Episode4). The regions sandwiched between two black lines are defined as the complex air pollution areas (CAPAs) where the mean daily PM$_{2.5}$ and MDA8 O$_3$ concentrations in BASE case are larger than 75 µg m^{-3} and 80 ppb. The calculated changes (percentage changes) averaged over CAPAs are also shown at the top of each panel.
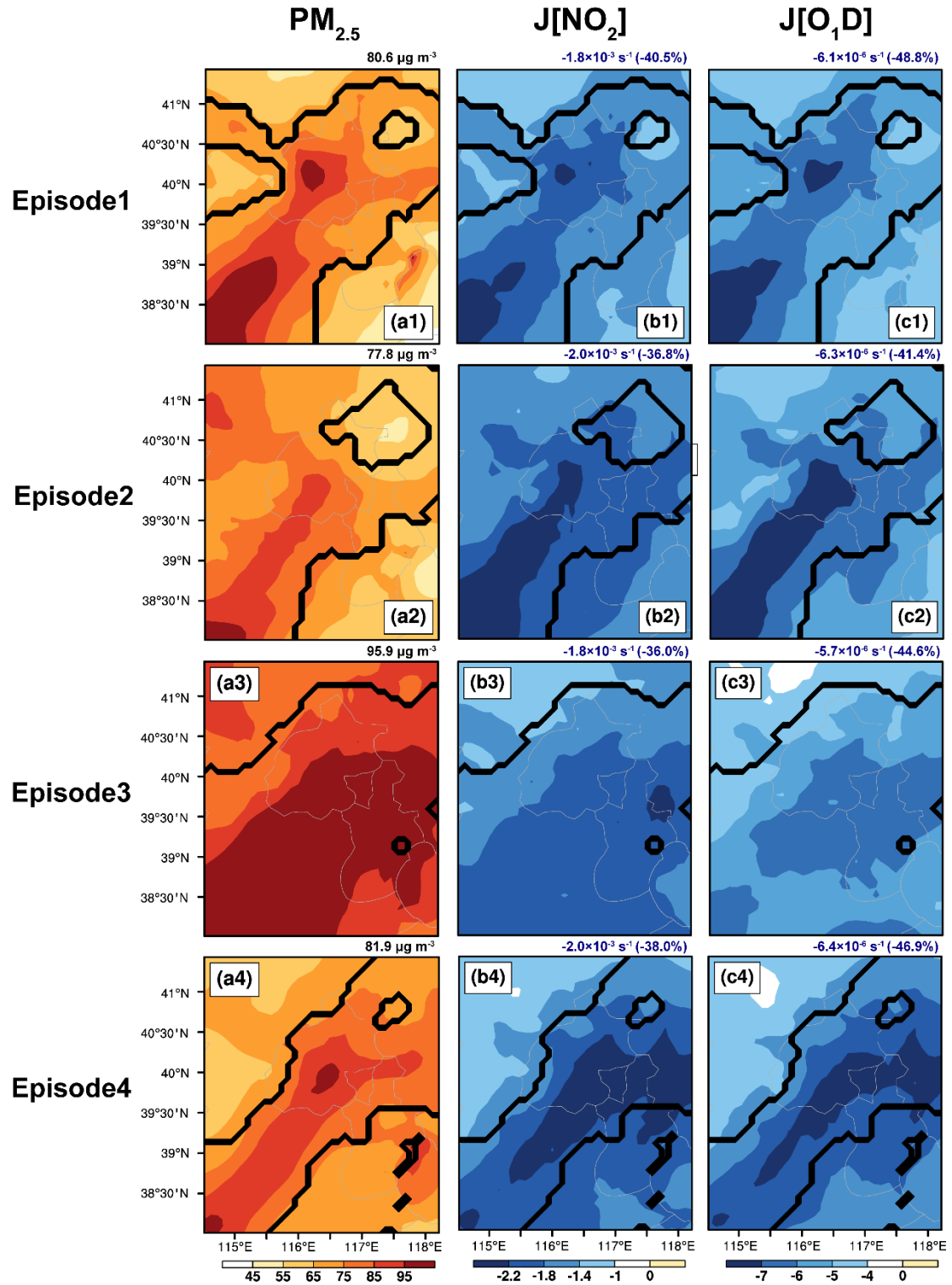
Figure 5. Spatial distributions of (a) simulated surface-layer $PM_{2.5}$ concentrations in BASE cases, and the changes in surface (b) $J[NO_2]$ and (c) $J[O^1D]$ due to aerosol-radiation interactions in the daytime (08:00-17:00 LST) during 28 July to 3 August 2014 (Episode1), 8-13 July 2015 (Episode2), 5-11 June 2016 (Episode3) and 28 June to 3 July 2017 (Episode4). The calculated values (percentage changes) avaraged over CAPAs are also shown at the top of each panel.

Figure 6. The changes in surface-layer ozone due to (a) aerosol-photolysis interaction (API), (b) aerosol-radiation feedback (ARF), and (c) the combined effects (ALL, defined as API+ARF) in the daytime (08:00-17:00 LST) during 28 July to 3 August 2014 (Episode1), 8-13 July 2015 (Episode2), 5-11 June 2016 (Episode3) and 28 June to 3 July 2017 (Episode4). The changes (percentage changes) in O_3 concentrations caused by API, ARF and ALL avaraged over CAPAs are also shown at the top of each panel.
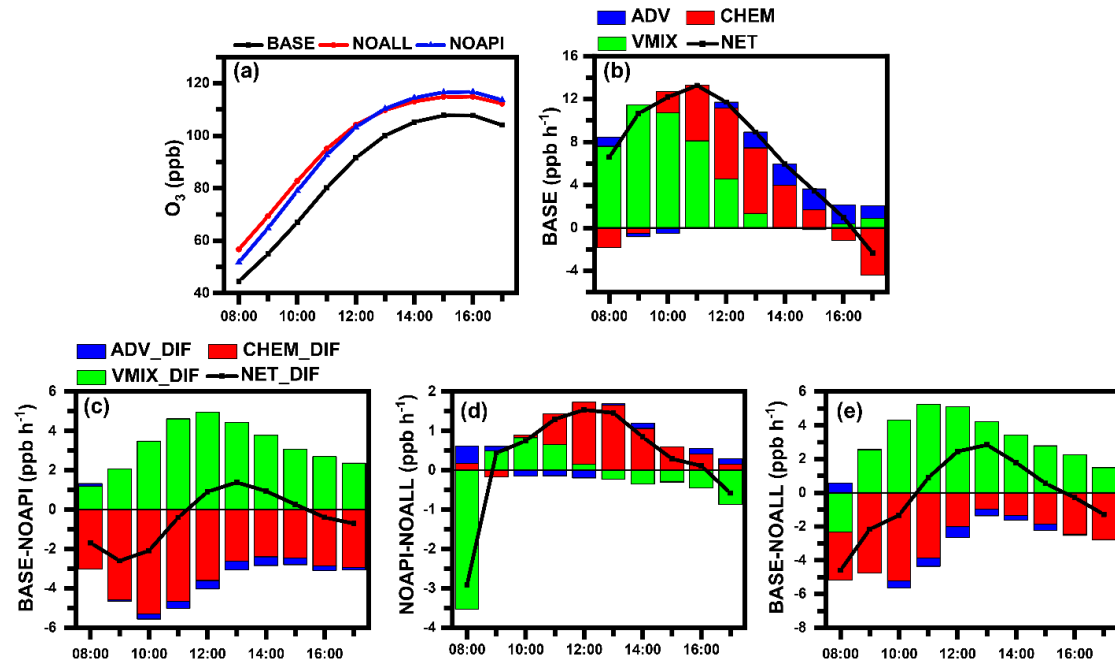
Figure 7. Temporal evolution characteristics of aerosol-radiation interactions on O_3 averaged over the four episodes. (a) Diurnal variations of simulated surface O_3 concentrations in BASE (black dotted line), NOAPI (blue dotted line), and NOALL (red dotted line) cases over CAPAs. (b) The hourly surface O_3 changes induced by each physical/chemical process using the IPR analysis method in BASE case. (c-e) Changes in hourly surface O_3 process contributions caused by API (BASE minus NOAPI), ARF (NOAPI minus NOALL), and ALL (BASE minus NOALL) over CAPAs during the daytime (08:00-17:00 LST). The black lines with squares denote the net contribution of all processes (NET, defined as VMIX+CHEM+ADV). Differences of each process contribution are denoted as VMIX_DIF, CHEM_DIF, ADV_DIF, and NET_DIF.
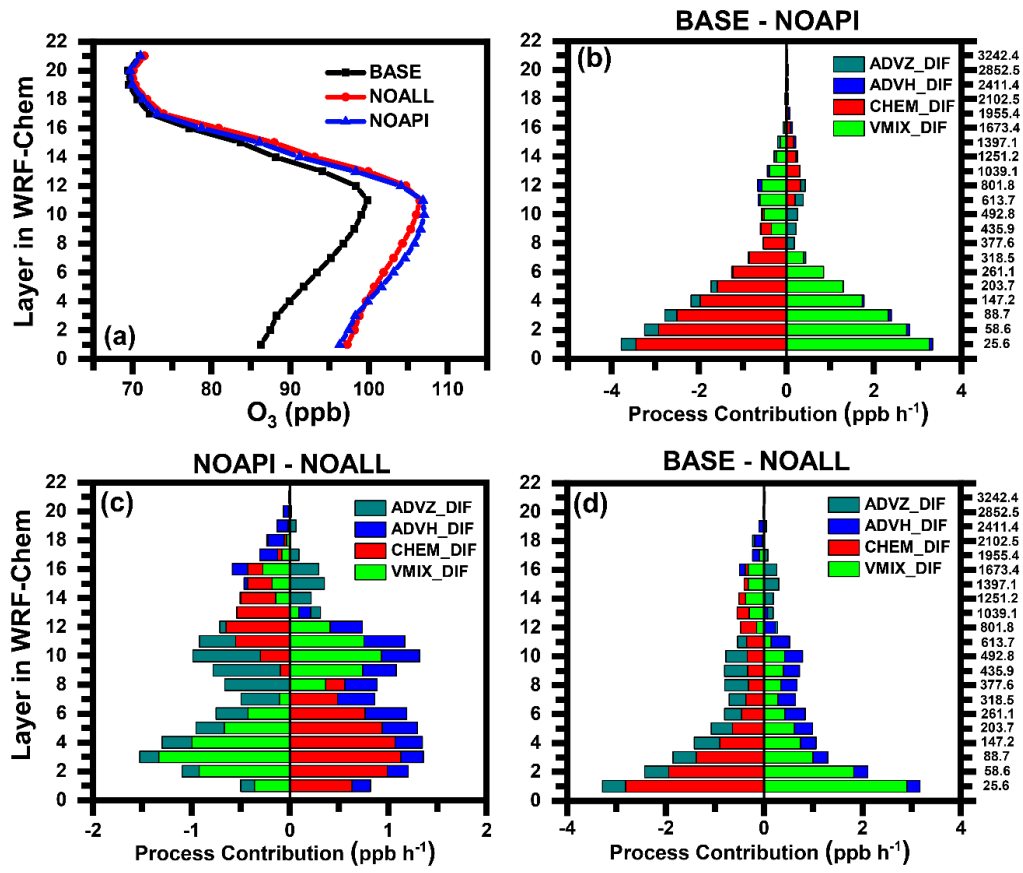
2 **Figure 8.** The impacts of aerosol-radiation interactions on vertical O_3 averaged over
3 the four episodes. (a) Vertical profiles of simulated O_3 concentrations in BASE (black
4 dotted line), NOAPI (blue dotted line), and NOALL (red dotted line) cases over
5 CAPAs. (b-d) Changes in O_3 budget due to API, ARF, and ALL over CAPAs during
6 the daytime (08:00-17:00 LST). Differences of each process contribution are denoted
7 by ADVZ_DIF, ADVH_DIF, CHEM_DIF, and VMIX_DIF.
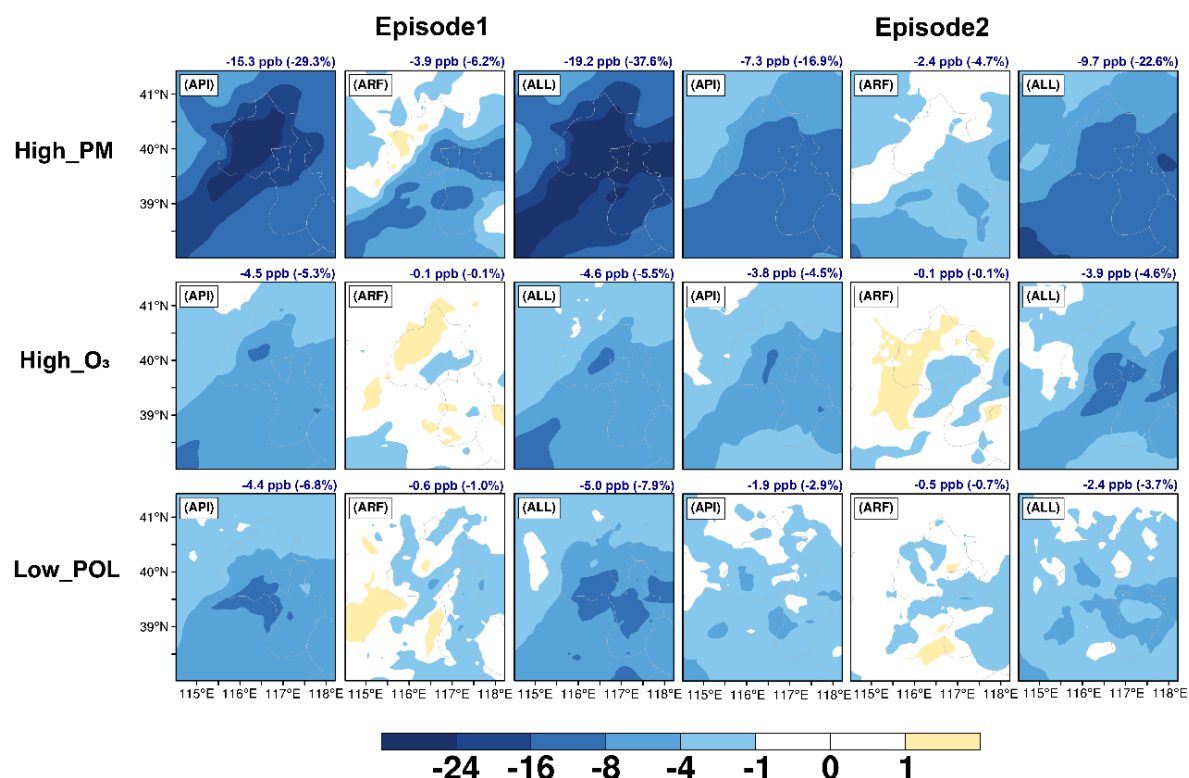
Figure 9. The changes in surface-layer O_3 due to aerosol-photolysis interaction (API), aerosol-radiation feedback (ARF), and the combined effects (ALL, API+ARF) in the daytime (08:00-17:00 LST) of 7-12 October 2014 (High_PM_Episode1), 7-11 April 2014 (High_PM_Episode2), 15-21 June 2017 (High_O$_3$_Episode1), 12-17 July 2017 (High_O$_3$_Episode2), 13-18 June 2016 (Low_POL_Episode1), and 13-17 July 2016 (Low_POL_Episode2). The changes (percentage changes) in O_3 concentrations caused by API, ARF and ALL avaraged over the entire simulated domain are also shown at the top of each panel.